Influence of solar-geomagnetic disturbances on SABER measurements of 4.3 μm emission and the retrieval of kinetic temperature and carbon dioxide

Christopher J. Mertens *

NASA Langley Research Center, 21 Langley Blvd., MS 401B, Hampton, VA 23681-2199, USA

Jeremy R. Winick and Richard H. Picard

Air Force Research Laboratories, Hanscom Air Force Base, Hanscom, MA 01731-3010, USA

David S. Evans

NOAA Space Weather Prediction Center, 325 Broadway, Boulder, CO 80303-0000, USA

Manuel López-Puertas

Instituto de Astrofisica de Andalucia, CSIC, Apdo. 3004, Granada 18080, Spain

Peter P. Wintersteiner

ARCON Corporation, 260 Bear Hill Rd., Waltham, MA 02451, USA

Xiaojing Xu

Preprint submitted to Elsevier Science *21 October 2008*

SSAI, Inc., 1 Enterprise Parkway, Hampton VA 23666, USA

Martin G. Mlynczak

NASA Langley Research Center, 21 Langley Blvd., MS 420, Hampton, VA 23681-2199, USA

James M. Russell III

Hampton University, 23 Tyler St., Hampton VA 23668, USA

Abstract

Thermospheric infrared radiance at 4.3 μm is susceptible to the influence of solar-geomagnetic disturbances. Ionization processes followed by ion-neutral chemical reactions lead to vibrationally excited NO^+ (i.e., $NO^+(v)$) and subsequent 4.3 μm emission in the ionospheric E-region. Large enhancements of nighttime 4.3 μm emission were observed by the TIMED/SABER instrument during the April 2002 and October-November 2003 solar storms. Global measurements of infrared 4.3 μm emission provide an excellent proxy to observe the nighttime E-region response to auroral dosing and to conduct a detailed study of E-region ion-neutral chemistry and energy transfer mechanisms. Furthermore, we find that photoionization processes followed by ion-neutral reactions during quiescent, daytime conditions increase the NO^+ concentration enough to introduce biases in the TIMED/SABER operational processing of kinetic temperature and CO_2 data, with the largest effect at summer solstice. In this paper, we discuss solar storm enhancements of 4.3 μm emission observed from SABER and assess the impact of $NO^+(v)$ 4.3 μm emission on quiescent, daytime retrievals of Tk/CO_2 from the SABER instrument.

* Corresponding author: Tel.: +1 757 864 2179; fax: +1 757 864 6326
Email addresses: Christopher.J.Mertens@nasa.gov (Christopher J. Mertens),

1 Introduction

The Thermosphere-Ionosphere-Mesosphere Energetics and Dynamics (TIMED) satellite was launched in December 2001. The primary objective of TIMED is to investigate and understand the energetics of the mesosphere, lower thermosphere and ionosphere (MLTI) region. Precipitating energetic particles induced by solar-geomagnetic disturbances rapidly and dramatically change the chemistry and thermal energy balance of the MLTI region. Several major solar eruptive events have occurred during TIMED mission operations. The two events considered in this paper are the April 2002 and the Halloween (October-November) 2003 solar storms. TIMED provides a suite of observations uniquely suited for investigating the response of the MLTI region to solar-geomagnetic disturbances. For example, data from the TIMED Global Ultraviolet Imager (GUVI) instrument have been used to analyze the total energy flux and characteristic energy of auroral electrons during the April 2002 storm (Christensen et al., 2003) and to investigate the causal mechanisms responsible for nighttime detached auroras during the Halloween 2003 storm (Zhang et al., 2005).

The Sounding of the Atmosphere using Broadband Emission Radiometry (SABER) instrument is an infrared limb sounder on the TIMED satellite

richard.picard@hanscom.af.mil, jeremy.winick@hanscom.af.mil (Jeremy R. Winick and Richard H. Picard), David.S.Evans@noaa.gov (David S. Evans), puertas@iaa.es (Manuel López-Puertas), winters@arcon.com (Peter P. Wintersteiner), xiaojing_xu@ssaihq.com (Xiaojing Xu), Martin.G.Mlynczak@nasa.gov (Martin G. Mlynczak), james.russell@hamptonu.edu (James M. Russell III).

(Russell et al., 1999). SABER provides global measurements of broadband infrared limb emission, which are analyzed to derive vertical profiles of kinetic temperature and key chemical species needed to quantify the radiative and chemical energy balance of the MLTI region. Large enhancements of thermospheric infrared emission were observed by several of the SABER radiometer channels during the April 2002 and Halloween 2003 solar storm events. Radiance enhancements observed in the 5.3 μm channel are due to emission from the vibration-rotation bands of nitric oxide (NO). The NO 5.3 μm emission is indicative of the conversion of solar energy to infrared radiation and represents a "natural thermostat" by which heat and energy are efficiently lost from the thermosphere to space and to the lower atmosphere. SABER 5.3 μm emission observations during the April 2002 storm and their subsequent interpretation in terms of energy loss were reported by Mlynczak et al. (2003, 2005).

Another thermospheric infrared spectral region subject to solar-geomagnetic influences is the 4.3 μm region, due to the vibration-rotation bands of NO^+ (Picard et al., 1987; Espy et al., 1988). During solar-geomagnetic storms, electron precipitation increases the ionization of the neutral atmosphere producing primarily N_2^+, O_2^+, O^+ and N^+ (e.g., Banks et al., 1974; Strickland et al., 1976). In the ionospheric E-region, these ions react with neutral species to produce NO^+ (Torr et al., 1990; Fox and Sung, 2001). Some of the ion-neutral reactions are exothermic enough to produce vibrationally excited NO^+, i.e., $NO^+(v)$ (Winick et al., 1987). The exothermic reactions are relatively fast. Above $\sim$ 110 km quenching of $NO^+(v)$ becomes less important and prompt emission of $NO^+(v)$ at 4.3 μm is a direct indication of auroral dosing in the E-region. The $NO^+(v)$ fundamental band (2344 cm^{-1}) is nearly coincident with the strong major isotopic $CO_2(\nu_3)$ band at 2349 cm^{-1}. Infrared emission at 4.3

μm during strong nighttime aurora can be enhanced by several orders of magnitude by $NO^+(v)$ compared to the background $CO_2(\nu_3)$ radiative emission. The E-region is largely inaccessible to in-situ observations and the SABER 4.3 μm measurements provide an excellent dataset to investigate the E-region response to solar-geomagnetic storms.

Infrared $NO^+(v)$ emission has important implications for the operational processing of SABER routine data products at high-latitudes near summer solstice, even for quiescent conditions. During daytime, kinetic temperature (Tk) and carbon dioxide (CO_2) volume mixing ratio (vmr) are simultaneously retrieved in version 1.06 data processing from SABER measurements of 15 μm and 4.3 μm limb emission, respectively (Mertens et al., 2002). Nighttime Tk is retrieved from 15 μm measurements using CO_2 data from the TIME-GCM climatology (Mertens et al., 2001, 2004). Solar EUV photons ionize the neutral atmosphere during the daytime, eventually leading to $NO^+(v)$ and emission at 4.3 μm through the exothermic ion-neutral reactions mentioned above. These processes are not included in the SABER operational Tk/CO_2 retrieval algorithm. Quiescent daytime thermospheric $NO^+(v)$ 4.3 μm emission is a small percentage of the background $CO_2(\nu_3)$ emission. However, 4.3 μm radiation transfer is strongly non-linear along the limb line-of-sight at mesospheric tangent heights, with non-negligible contributions coming from the lower thermosphere. Consequently, weak atmospheric emission from $NO^+(v)$ not accounted for in the Tk/CO_2 retrieval algorithm can have a rather significant effect on retrieved CO_2 throughout the MLTI region, which subsequently introduces a bias in retrieved Tk. Most of the SABER data products require temperature as input into their respective retrieval algorithms. Thus, a bias in Tk introduces biases in nearly all of the SABER data products. We have evidence, from

a combination the SABER CO_2 data and model simulations, that strongly suggests that quiescent 4.3 μm emission by $NO^+(v)$ is introducing errors in retrieved Tk/CO_2 at high latitudes, with the largest effect at summer solstice.

The focus of this paper is on $NO^+(v)$ 4.3 um emission during both quiescent and geomagnetically disturbed conditions. We present SABER observations of nighttime auroral enhancements of 4.3 μm emission during the April 2002 and Halloween 2003 storms. We conduct a preliminary assessment of the impact of quiescent daytime $NO^+(v)$ 4.3 μm emission on high-latitude SABER Tk/CO_2 retrievals.

2 Solar Storm Enhancements of 4.3 μm Emission

Nighttime enhancements of 4.3 μm emission can be several orders of magnitude during strong aurora. Figure 1 shows representative radiance profiles measured by the SABER (channel 7) 4.3 μm radiometer channel during the April 2002 and Halloween 2003 solar storms. The vertical, dashed line in the figure is the channel 7 noise equivalent radiance (NER), which is 7.35 x 10^{-7} W/m^2/sr. Prior to the onset of the storm periods, the radiance decreases with increasing altitude reaching the detector noise level by $\sim$ 135 km. During the peak of the solar storms, the 4.3 μm radiance is enhanced by up to several orders of magnitude and doesn't reach the detector noise level until well above 180 km. The storm-enhanced radiance profile during the Halloween 2003 event in Figure 1 has the same slope as its corresponding pre-storm radiance profile, while this is not the case for the April 2002 storm event. The correlation between the slope of the storm and pre-storm radiance profiles during the Halloween event is fortuitous, since the vertical profile of the storm-enhanced radiance profile

depends on the specific mapping of the auroral electron energy spectrum on the ionization rate profile and subsequent ion-neutral compositions.

Figure 2 shows a comparison of nighttime precipitating total electron energy flux with SABER-derived $NO^+(v)$ Volume Emission Rate (VER) at 110 km in the northern hemisphere. The $NO^+(v)$ VER is the quantity that characterizes the storm-time enhancement of 4.3 μm emission (see section 3.1 and Mertens et al. (2007a, 2007b)). The total electron energy flux is determined from measurements made by the National Oceanic and Atmospheric Administration (NOAA) Total Energy Detector (TED) instruments onboard the Polar Orbiting Environmental Satellites (POES). The NOAA/POES satellites are in sun-synchronous orbits. POES-17 is in an orbit that crosses the equator northbound at 2215 local time at the sub-satellite point. As a result, POES-17 covers the northern hemisphere auroral zone in the time sector ranging from about 2000 local time through 0100 local times. POES-15 and POES-16 cross the equator at about 1900 and 1400 local times at the sub-satellite points. Thus, they sample the northern hemisphere largely during the daytime hours. The satellite coverage described above is opposite in the southern hemisphere. The total electron energy flux is derived from POES directional energy flux measurements over the energy range from 50 eV to 20 keV. Auroral electrons with these energies deposit their energy at altitudes above 100 km (Rees, 1989).

The SABER and POES data in Figure 2 were taken during the Halloween 2003 storm event on 30 October. The data are presented in polar magnetic coordinates (magnetic latitude and magnetic local time (MLT)). A continuous distribution of total electron energy flux was obtained by binning and averaging the POES data on a 1x2x3 magnetic latitude (degrees), magnetic

longitude (degrees), and UT-time (hours) grid. The gridded POES data are interpolated to fill in all magnetic longitude grid points. The corresponding MLT are determined by the geocentric-magnetic coordinate transformation. The SABER $NO^+(v)$ VER are shown at 110 km for each orbit that falls within the 3-hour UT-time intervals shown for the corresponding POES data. Auroral precipitation changes rapidly in space and time. Nevertheless, one can observe from Figure 2 that high (low) levels of auroral precipitation generally correspond to high (low) levels of $NO^+(v)$ VER.

Thus, thermospheric infrared emission at 4.3 μm is an excellent proxy for observing the ionospheric E-region response to strong nighttime auroral dosing. The combination of SABER 4.3 μm radiance measurements, observations of precipitating electron energy characteristics, ionospheric chemistry and radiation transfer models, can be used to conduct a detailed investigation of our understanding of the physical mechanisms responsible for the E-region energetics and the response to auroral electron dosing, since many of these mechanisms and their subsequent rates of reactions are still largely uncertain (Winick et al., 1987). This work is currently under investigation (Mertens et al., 2007a, 2007b, 2008b). In the next section we briefly summarize our $NO^+(v)$ energetics model. In section 4 our model simulations are used to assess the impact of quiescent, daytime $NO^+(v)$ 4.3 μm emission on the SABER Tk/CO_2 version 1.06 retrievals for high-latitude summer solstice conditions.

3 NO^+(v) Energetics Model

3.1 NO^+(v) Kinetics and Chemistry

A number of ion-neutral reactions are sufficiently exothermic to produce vibrationally excited NO^+ (Winick et al., 1987; Caledonia et al., 1995; Dothe et al., 1996; Smith et al., 2000). The reactions that have received the most attention are as follows:

$$\begin{aligned}
N_2^+ + O &\rightarrow NO^+(\nu) + N(^4S) + 3.08 \text{ eV } (\nu_{max} = 10) \\
&\rightarrow NO^+(\nu) + N(^2D) + 0.69 \text{ eV } (\nu_{max} = 2) \qquad (1) \\
N^+ + O_2 &\rightarrow NO^+(\nu) + O(^1S) + 2.43 \text{ eV } (\nu_{max} = 8) \\
&\rightarrow NO^+(\nu) + O(^1D) + 4.66 \text{ eV } (\nu_{max} = 18) \\
&\rightarrow NO^+(\nu) + O(^3P) + 6.63 \text{ eV } (\nu_{max} = 28) \qquad (2) \\
O^+ + N_2 &\rightarrow NO^+(\nu) + N(^4S) + 1.1 \text{ eV } (\nu_{max} = 3) \qquad (3) \\
O_2^+ + NO &\rightarrow NO^+(\nu) + O_2(X) + 2.83\text{eV } (\nu_{max} = 9) \\
&\rightarrow NO^+(\nu) + O_2(a) + 1.85 \text{ eV } (\nu_{max} = 6) \\
&\rightarrow NO^+(\nu) + O_2(b) + 1.20 \text{ eV } (\nu_{max} = 4). \qquad (4)
\end{aligned}$$

Loss of NO^+(v) is by collisional quenching and spontaneous radiative emission. The quenching and radiative loss processes are represented by

$$\begin{aligned}
NO^+(\nu) + N_2(v = 0) &\rightleftharpoons NO^+(\nu - 1) + N_2(v = 0) \qquad (5) \\
NO^+(\nu) &\rightarrow NO^+(\nu - 1) + h\nu. \qquad (6)
\end{aligned}$$

Reaction (2) is the only one for which the vibrational distributions of the products have been measured in the laboratory (Smith et al., 1983; denoted SM83 in Table 1). Albritton et al. (1979) and Langford et al. (1986) determined the branching ratios for electronically excited atomic oxygen atoms formed by reaction (2), and Smith et al. deduced the fractional rate that populates $\nu = 1 - 14$. Reaction (2) is an important contributor to NO^+(v) 4.3 μm

emission below $\sim$ 140 km (Winick et al., 1987; Caledonia et al., 1995). In our analysis, we assume the total reaction rate and fractional vibrational state distribution are those obtained by the above measurements.

Above 140 km, reaction (1) dominates the production of NO^+(v) and subsequent 4.3 μm emission (Winick et al., 1987; Caledonia et al., 1995; Dothe et al., 1996; Smith et al., 2000). However, the vibrational distribution of NO^+(v) from (1) has never been measured in the laboratory. On the other hand, modeling of NO chemistry and analysis of high-resolution atmospheric emission spectra suggest that N(^{2}D) is the dominant channel in reaction (1) (Winick et al., 1987; Dothe et al., 1996). There are a number of assumptions for the vibrational state distribution reported in the literature. We assume the nominal case utilized by Winick et al. (1987) (denoted WK87 in Table 1), where the vibrational state distribution is given by f(ν=0) = 0.25, f(ν=1) = 0.50, and f(ν=2) = 0.25. For the total rate of reaction we use the rate coefficient measured by McFarland et al. (1974) (denoted MF74 in Table 1).

Reaction (3) has received attention recently as a candidate for non-thermal rotational excitation of NO^+(ν,J) (Smith et al., 2000; and Duff and Smith, 2000). Smith et al. (2000) analyzed CIRRIS 1A data and showed that most of the NO^+ produced by reaction (3) is rotationally thermalized below 150 km. Furthermore, reaction (3) is not a dominant contributor to the overall production of NO^+(v) below $\sim$ 160 km. Model studies conducted by Duff and Smith (2000) showed that NO^+(v) atmospheric radiance from reaction (3) was dominated by ν =1 emission. Taking these results into consideration, and restricting our analysis to altitudes below $\sim$ 160 km, we assume rotational LTE for this reaction and assume that NO^+ is created in vibrational state ν = 1 (denoted DS00 in Table 1). We also use the reaction rate coefficient measured

by McFarland et al. (1973) (denoted MF73 in Table 1), as suggested by Smith et al. (2000).

The large exothermicity of reaction (4) makes the production of $NO^+(v)$ possible. This process is important for high [NO], which occurred during the recent solar storm events (Richards, 2004; Mlynczak et al, 2003). However, there were no previous observation-based studies that presented evidence of $NO^+(v)$ excitation and subsequent 4.3 μm emission from this reaction. On the contrary, in a recent study we found this reaction to be the dominant source of $NO^+(v)$ excitation and auroral 4.3 μm emission below 160 km (Mertens et al., 2008b). The total rate coefficient for reaction (4) is obtained from the measurements of Lindinger et al. (1974) (denoted LD74 in Table 1). The nascent $NO^+(v)$ distribution from this reactions is given by Mertens et al. (2008b) (denoted MT08 in Table 1). However, since we are considering quiescent conditions in this paper, we ignore this reaction in the subsequent analysis.

Collisional quenching of $NO^+(v)$ in (5) is negligible above 130 km, but becomes an important loss mechanism by 110 km (Winick et al., 1987). Dobler et al. (1983) (denoted DO83 in Table 1) and Federer et al. (1985) measured similar rate coefficients for the quenching of $NO^+(\nu{=}1)$ in neutral collisions. Quenching rates of levels with $\nu > 1$ have not been measured. As a result, various quenching schemes have been assumed in the literature. We use the scheme of Winick et al. (1987), where quenching of $NO^+(v)$ is by collisions with N_2 and single-quantum quenching is assumed for all $NO^+(v)$ levels.

Radiative loss of $NO^+(v)$ in (6) is modeled using the Einstein A-coefficients reported by Werner and Rosmus (1982), who calculated spontaneous emission rates for the fundamental and first two overtone emission sequences for $\nu =$

1 to $\nu = 20$. We use the fundamental ($\Delta\nu$=1) and the first overtone ($\Delta\nu$=2) A-coefficients, as the second overtone spontaneous emission rates are much smaller than the $\Delta\nu$=1 and $\Delta\nu$=2 rates.

The reactions rate coefficients, vibrational state distributions, collisional and radiative loss rates described in this section allow one to calculate the steady-state NO^+ vibrational state populations, provided one knows the ion and neutral concentrations that appear on the left-hand side of reactions (1)-(4). In our $NO^+(v)$ energetics model, the ion/neutral concentrations are calculated using the FLIP model, as described in the next subsection.

3.2 FLIP Model

The field-line interhemispheric plasma (FLIP) model is a one-dimensional ionosphere and thermosphere model that calculates plasma densities and temperatures along entire magnetic flux tubes from below 100 km in one hemisphere, through the plasmasphere to below 100 km in the conjugate hemisphere (Richards, 2002). The equations solved along the flux tubes are the time-dependent continuity and momentum equations for O^+, H^+, He^+, and N^+. The electron and ion temperatures are obtained by solving the energy equation. Chemical equilibrium densities are calculated for NO^+, O_2^+, N_2^+, $O^+(^2P)$, and $O^+(^2D)$ ions below 500 km in each hemisphere. The densities of minor neutral species NO, $O(^1D)$, $N(^2D)$, and $N(^4S)$ are obtained by solving the time-dependent continuity and momentum equations from 100 to 500 km in each hemisphere. The model also solves for the first five vibrational levels of molecular nitrogen ($N_2(v)$).

We use the FLIP model in the simulations of $NO^+(v)$ 4.3 μm emission. FLIP provides the ion/neutral species for the reactants in (1)-(3). Figure 3 shows results from FLIP simulations. The ion concentrations needed to calculate the $NO^+(v)$ populations are shown in the left-hand column. The right-hand column are the neutral concentrations. The first row is a simulation for a quiet day (8 April) prior to the onset of the April 2002 solar storm. The second row is a simulation of the ion/neutral concentrations for a representative day (20 April) during the peak thermospheric infrared response to the April 2002 storm, with auroral dosing similar to the total electron energy flux observed by the NOAA/POES instruments during this storm. Notice that the NO^+ concentration for the auroral dosing is approximately two orders of magnitude greater than the concentration during the undisturbed day. The enhancement in the NO^+ concentration for the simulation in Figure 3 is similar to the enhancement of thermospheric 4.3 μm radiance observed by SABER during the solar storms (see Fig. 1).

Figure 4 shows a comparison of FLIP electron density (i.e., [e]) simulations at 115 km with ground-based VHF incoherent scatter radar measurements of electron density taken by the European Incoherent SCATer (EISCAT) facility at Tromsø, Norway (70N, 19E). We compare FLIP/EISCAT [e] during a period of low geomagnetic activity and continuous EISCAT measurements from June 14-19, 2004. FLIP [e] simulations are in excellent agreement with the 1-hour averaged EISCAT [e] measurements during the daytime hours. The largest differences occur over several hours near midnight MLT due to 'quiet-time' auroral activity. A geomagnetic substorm appears to have occurred on June 16 (Akasofu, 1964), which can be associated with particle precipitation (parameterized by the Hemispheric Power (HP) index), enhanced electric

fields with both field-aligned and electrojet currents (parameterized by the AE-index). However, we are analyzing quiescent, daytime conditions in this paper and Figure 4 demonstrates the efficacy of using FLIP to simulate the E-region plasma under these conditions at high-latitude.

3.3 Infrared Radiance Model

The SABER 4.3 μm limb emission can be modeled once the $NO^+(v)$ populations are computed, which are calculated using the FLIP model and the $NO^+(v)$ kinetics and chemistry model described in sections 3.2 and 3.1, respectively. The $CO_2(\nu_3)$ contribution to the SABER 4.3 μm measurements is modeled using the 4.3 μm channel forward model component of the operational non-LTE Tk/CO_2 retrieval algorithm (Mertens et al., 2002). The forward model is comprised of two parts: (1) the CO_2 vibrational temperature (Tv) model and (2) the limb radiance model. Limb radiance is calculated using BANDPAK (Marshall et al., 1994), which is based on emissivity databases calculated line-by-line using LINEPAK routines (Gordley et al., 1994). The CO_2 Tv model is based on the Modified Curtis Matrix approach (López-Puertas et al., 1986a-b, 1998), and uses BANDPAK in all the radiation transfer calculations.

The in-band SABER $NO^+(v)$ 4.3 μm limb radiance will be simulated using LINEPAK, radiative line parameters from the HITRAN 2000 molecular spectroscopic database (Rothman et al., 2003), the SABER 4.3 μm channel relative spectral response filter, and $NO^+(v)$ Tv's (or equivalently, the $NO^+(v)$ populations) calculated using FLIP and the $NO^+(v)$ kinetics and chemistry model. The HITRAN $NO^+(v)$ line parameters are derived from the spectroscopic con-

stants and parameters calculated by Billingsley (1973), Huber and Herzberg (1979), and Werner and Rosmus (1982). Figure 5 is a simulation of infrared 4.3 μm limb emission for quiet and disturbed conditions. The disturbed condition is for auroral dosing representative of the total electron energy flux measured by the NOAA/POES instruments during the April 2002 solar storm. Clearly, NO^+(v) dominates the 4.3 μm spectrum. The black curve is the SABER spectral response filter. The SABER in-band contributions from NO^+(v) is 60 to 80% of the SABER 4.3 μm channel radiance for the simulation in Figure 5. The SABER in-band NO^+(v) 4.3 μm emission is comprised of $NO^+(\Delta\nu{=}1)$ transition from $\nu = 1$ to 4.

3.4 Auroral Excitation of $N_2(v)$

Auroral electrons vibrationally excite molecular nitrogen by (1) inelastic collisions between low energy secondary electrons and N_2 (Newton et al., 1974), and (2) chemical reactions (Richards, 2002). Reaction (3) is highly dependent on the vibrational level of N_2 and can significantly increase the effective reaction rate in the F2 region. These mechanisms are included in the FLIP model.

Auroral excitation of $N_2(\nu)$ also affects local 4.3 μm emission from $CO_2(\nu_3)$ below about 110 km through V-V exchange between $CO_2(\nu_3)$ and $N_2(\nu)$:

$$CO_2(\nu_3) + N_2(\nu) \leftrightarrow CO_2(\nu_3 - 1) + N_2(\nu + 1) + 18 \text{ cm}^{-1} \quad (7)$$

Reaction (7) was measured by Inoue and Tsuchiya (1975) for $N_2(\nu{=}1)$.

Above 110 km, $N_2(\nu)$ is quenched by collisions with atomic oxygen and locally

decouples from $CO_2(\nu_3)$. However, aurora can potentially influence $CO_2(\nu_3)$ 4.3 μm emission above 110 km through non-local processes due to V-V exchange between $CO_2(\nu_3)$ and $N_2(\nu)$ below 110 km followed by radiative transport to higher altitudes.

The influence of auroral electron excitation of $N_2(\nu)$ on 4.3 μm emission is not included in the simulations presented in this paper. Our studies have shown that auroral $CO_2(\nu_3)$ 4.3 μm emission to be insignificant in comparison to auroral NO^+(v) 4.3 μm emission, consistent with the results found by O'Neil et al. (2007). This is especially true for the quiescent daytime conditions considered in this paper.

4 Influence of NO^+(v) 4.3 μm Emission on SABER Tk/CO_2 Retrievals

Representative SABER version 1.06 monthly zonal mean CO_2 vmr data are shown in Figure 6 for winter, equinox, and summer seasons. Comparisons of SABER CO_2 vmr with TIME-GCM (Roble, 1995) model-generated climatological data show that SABER CO_2 vmr is systematically lower than the model simulations at all altitudes above roughly 70-75 km (Mertens et al., 2008a). This result is consistent with previous CO_2 vmr measurements determined from atmospheric infrared remote sensing observations (Kaufmann et al, 2002; Zaragoza et al., 2000; López-Puertas et al., 2000; and references therein). However, the puzzling feature in Figure 5 is the meridional gradient in the CO_2 concentration near the polar regions not seen in the model data, which dramatically increases from equinox to summer season. In fact, there is a step-function feature in the July SABER data coincident with the latitude

region of the auroral oval. Simulations from our $NO^+(v)$ energetics model suggest that the step-function feature in the CO_2 data is caused by $NO^+(v)$ 4.3 μm emission, which is not accounted for in the operational SABER non-LTE Tk/CO_2 retrieval algorithm.

The omission of the $NO^+(v)$ contribution to the 4.3 μm radiance in the Tk/CO_2 retrieval algorithm underestimates the radiation transfer modeling of the SABER 4.3 μm channel measurement, which in turn results in an overestimation of CO_2. Taking the northern hemisphere in Figure 6 as an example, the polar region is exposed to increasing periods and intensity of solar illumination as the seasons proceed from winter (January) to summer (July). Subsequently, the polar region NO^+ concentrations increase from winter to summer as the rate of photoionization and photoelectron concentrations increase (Mertens et al., 2008a). The overestimated CO_2 concentration near summer solstice (i.e., the July SABER data) is coincident with the auroral oval latitude band due to the geometric effects of Earth's magnetic field on the photoelectrons that participate in the E-region chemistry leading to NO^+.

Figure 7 is a simulation of the SABER 4.3 μm channel measurements with and without $NO^+(v)$ 4.3 μm emission included. The simulated observations are for five SABER measurement profiles near 69N on 4 July, 2002. The $NO^+(v)$ 4.3 μm emission was calculated using the $NO^+(v)$ energetics model described in section 3. As shown in Figure 7, $NO^+(v)$ contributes $\sim 1\%$ of the total limb radiance near 110 km and between 6-8% at 130 km. These simulations are consistent with the $NO^+(v)$ contribution to 4.3 μm emission determined from the spectral radiance observations made by the MIPAS (Michelson Interferometer for Passive Atmospheric Sounding) instrument on the ENVISAT-1 satellite (López-Puertas, private communications, 2004). This consistency gives us

some confidence in our $NO^+(v)$ energetics model.

The $NO^+(v)$ contribution to the daytime 4.3 μm emission has a significant effect on the CO_2 retrieval. Because of the severe non-linearity in the 4.3 μm radiation transfer, the weighting functions in the mesosphere extend up into the lower thermosphere, with non-negligible contributions arising from the 130 km region (Mertens et al., 2008a). Thus, the CO_2 retrieval can be overestimated throughout the mesosphere as a result of relatively weak $NO^+(v)$ 4.3 μm emission contributions above $\sim$ 110 km.

An overestimation of CO_2 will cause an underestimation in Tk. The low bias in Tk was estimated by forcing the non-LTE Tk/CO_2 retrieval algorithm to use the SABER-CO_2 mean profile at 41N. The TIME-GCM model results suggest that the CO_2 vmr in the northern polar region for summer solstice should be roughly the same as the CO_2 vmr at mid-latitudes. CO_2 validation studies (Mertens et al. 2008a) give us confidence in the SABER CO_2 data at mid-latitudes. Temperature retrievals in the polar summer region with the anomalously large CO_2 profiles (i.e., Figure 6) versus using the SABER-CO_2 mean profile at 41N should give a reasonable assessment of the Tk bias due to $NO^+(v)$ 4.3 μm emission. The result of this sensitivity study is shown in Figure 8.

The sensitivity study in Figure 8 indicates a low bias in polar summer Tk of about 5 K in the upper mesosphere, which is centered in altitude at 80 km. Above 100 km, the bias is much larger. The bias in Tk will introduce errors in most of the other SABER data products.

5 Summary

Large enhancements of thermospheric infrared emission was observed by SABER during the recent superstorm events: the April 2002 and the Halloween 2003 solar storms. Radiance enhancements in the SABER 4.3 μm channel are due to vibrationally excited NO^+, which is an excellent proxy for observing the ionospheric E-region response to auroral electron dosing induced by solar-geomagnetic disturbances. An NO^+(v) energetics model was developed to simulate the exothermic ion-neutral reactions that produce NO^+(v) and the subsequent emission at 4.3 μm. Efforts are underway to use this model along with SABER 4.3 μm limb radiance observations and electron energy characteristics measured by the NOAA/POES satellites to investigate E-region ion-neutral chemistry and energy transfer mechanisms (Mertens et al., 2007a, 2007b, 2008b).

NO^+(v) 4.3 μm emission during quiescent, daytime conditions introduce biases in version 1.06 SABER-retrieved Tk/CO_2 at high-latitudes in the mesosphere and lower thermosphere. The impact of NO^+(v) 4.3 μm emission on retrieved CO_2 is maximum for summer solstice conditions, moderate for equinox, and negligible for winter conditions. The NO^+(v) contribution to SABER 4.3 μm channel measurements for polar summer solstice is 1% at 110 km and 6-8% at 130 km, consistent with analysis of MIPAS 4.3 μm spectral radiance measurements. The NO^+(v) contribution to the SABER 4.3 μm observations results in an overestimation of retrieval CO_2 which subsequently induces a low bias in retrieved Tk by 5 K near 80 km, with much larger biases above 100 km. The temperature biases will introduce errors in most of the other SABER data products.

References

Akasofu, S.-I., The development of the auroral substorm, Planet. Space Sci., 12(4), 273-282, 1964.

Albritton, D. L., A. A. Viggiano, I. Dotan, and F. C. Fehsenfeld, Production of $NO^+(a^3\Sigma^+)$ ion in the reaction of N^+ ions with O_2 at 300 K, J. Chem. Phys., 71(8), 3295-3298, 1979.

Banks, P. M., C. R. Chappell, and A. F. Nagy, A new model of the interaction of auroral electrons with the atmosphere: Spectral degradation, backscatter, optical emission, and ionization, J. Geophys. Res., 79(10), 1459-1470, 1974.

Billingsley II, F. P., Calculation of the absolute infrared intensities for the 0-1, 0-2, and 1-2 vibration-rotation transitions in the ground state of NO^+, Chem. Phys. Lett., 23(2), 160-166, 1973.

Caledonia, G. E., R. E. Murphy, R. M., Nadile, and A. J. Ratkowski, Analysis of auroral infrared emission observed during ELIAS experiment, Ann. Geophysicae, 13, 247-252, 1995.

Christensen, A. B., et al., Initial observations with the Global Ultraviolet Imager (GUVI) in the NASA TIMED satellite mission, J. Geophys. Res., 108(A12), 1451, doi:10.1029/2003JA00918, 2003.

Dobler, W., W. Federer, F. Howorka, W. Lindinger, M. Durup-Ferguson, and E. Ferguson, Vibrational relaxation of $NO^+(v)$ ions in neutral collisions, J. Chem. Phys., 79(3), 1543-1544, 1983.

Dothe, H., F. von Esse, and R. D. Sharma, Rotational temperatures and production mechanisms of some infrared radiators in the daylit terrestrial thermosphere, J. Geophys. Res., 101(A9), 19,715-19,721, 1996.

Duff, J. W., and D. R. Smith, The $O^+(^4S)+N_2(X^1\Sigma_g^+) \rightarrow NO^+(X^1\Sigma^+) + N(^4S)$ reaction as a source of highly rotationally excited NO^+ in the thermosphere,

J. Atmos. Solar-Terr. Phys., 62, 1199-1206, 2000.

Espy, P. J., C. R. Harris, A. J. Steed, J. C. Ulwick, and R. H. Haycock, Rocketborne interferometer measurement of infrared auroral spectra, Plant. Space Sci., 36, 543-551, 1988.

Federer, W., W. Dopler, F. Howorka, and W. Lindinger, Collisional relaxation of vibrationally excited NO^+(v) ions, J. Chem. Phys., 83(3), 1032-1028, 1985.

Fox, J. L., and K. Y. Sung, Solar activity variations of the Venus thermosphere/ionosphere, J. Geophys. Res., 106(A10), 21,305-21,335, 2001.

Gordley, L. L., B. T. Marshall, and D. A. Chu, LINEPAK: Algorithms for modeling spectral transmittance and radiance, J. Quant. Spectrosc. Radiat. Transfer, 52(5), 563-580, 1994.

Huber, K. P., and G. Herzberg, Molecular Spectra and Molecular Structure IV. Constants of Diatomic Molecules, Van Nostrand Reinhold, New York, 1979.

Inoue, G., and S. Tsuchiya, Vibration-vibration energy transfer of $CO_2(00^01)$ with N_2 and CO at low temperatures, J. Phys. Soc. Jpn., 39, 386-479, 1975.

Kaufmann, M., O. A. Gusev, K. U. Grossmann, R. G. Roble, M. E. Hagan, C. Hartsough, and A. A. Kutepov, The vertical and horizontal distribution of CO_2 densities in the upper mesosphere and lower thermosphere as measured by CRISTA, J. Geophys. Res., 107(D23), 8182, doi: 10.1029/2001JD000704, 2002.

Langford, A. O., V. M. Bierbaum, and S. R. Leone, Branching ratios for electronically excited oxygen atoms formed in the reaction of N^+ with O_2 at 300 K, J. Chem. Phys., 84(4), 2158-2166, 1986.

Lindinger, W., F. C. Fehsenfeld, A. L. Schmeltekopf, and E. E. Ferguson, Temperature dependence of some ionospheric ion-neutral reactions from

300-900 K, J. Geophys. Res., 79(31), 4753-4756, 1974.

López-Puertas, M., R. Rodrigo, A. Molina, and F. W. Taylor, A non-LTE radiative transfer model for infrared bands in the middle atmosphere. I. Theoretical basis and application to CO_2 15 μm bands, J. Atmos. Terr. Phys., 48(8), 729-748, 1986a.

López-Puertas, M., R. Rodrigo, J. J. López-Moreno, and F. W. Taylor, A non-LTE radiative transfer model for infrared bands in the middle atmosphere. II. CO_2 (2.7 and 4.3 μm) and water vapor (6.3 μm) bands and $N_2(1)$ and $O_2(1)$ vibrational levels, J. Atmos. Terr. Phys., 48(8), 749-764, 1986b.

López-Puertas, M., G. Zaragoza, M. A. López-Valverde, and F. W. Taylor, Non local thermodynamic equilibrium (LTE) atmospheric limb emission at 4.6 μm 1. An update of the CO_2 non-LTE radiative transfer model, J. Geophys. Res., 103(D7), 8499-8513, 1998.

López-Puertas, M., M. A. Lopez-Valverde, R. R. Garcia, and R. G. Roble, A review of CO_2 abundances in the middle atmosphere, Geophysical Monograph 123, pp. 83-100, American Geophysical Union, Washington DC, 2000.

Marshall, B. T., L. L. Gordley, and D. A. Chu, BANDPAK: Algorithms for modeling broadband transmission and radiance, J. Quant. Spectrosc. Radiat. Transfer, 52(5), 581-599, 1994.

McFarland, M., D. L. Albritton, F. C. Fehsenfeld, E. E. Ferguson, and A. L. Schmeltekopf, Flow-drift technique for ion mobility and ion-molecule reaction rate constant measurements. II. Positive ion reactions of N^+, O^+, and N_2^+ with O_2 and O^+ with N_2 from thermal to $\sim$ 2 eV, J. Chem. Phys., 59(12), 6620-6628, 1973.

McFarland, M., D. L. Albritton, F. C. Fehsenfeld, E. E. Ferguson, and A. L. Schmeltekopf, Energy dependence and branching ratio of the $N2^+$ + O reaction, J. Geophys. Res., 79(19), 2925-2926, 1974.

Mertens, C. J., et al., Kinetic temperature and carbon dioxide from measurements of broadband Earth limb emission measurements taken from the TIMED/SABER instrument, Adv. Space Res., doi:10.10106/j.asr.2008.04.017, 2008a.

Mertens, C. J., J. R. Fernandez, X. Xu, D. S. Evans, M. G. Mlynczak, and J. M. Russell III, A new source of auroral infrared emission observed by TIMED/SABER, Geophy. Res. Lett., 35, L17106, doi:10.1029/2008GL034701, 2008b.

Mertens, C. J., J. C. Mast, J. R. Winick, J. M. Russell III, M. G. Mlynczak, and D. S. Evans, Ionospheric E-region response to solar-geomagnetic storms observed by TIMED/SABER and application to IRI storm-model development, Adv. Space Res., 39, 715-728, 2007a.

Mertens, C. J., J. R. Winick, J. M. Russell III, M. G. Mlynczak, D. S. Evans, D. Bilitza, and X. Xu, Empirical storm-tiem correction to the international reference ionosphere model E-region electron and ion density parameterizations using observations from TIMED/SABER, *Proceedings of SPIE, Remote Sensing of Clouds and Atmosphere VII*, Florence, Italy, September 17-19, vol. 6745, 65451L, doi:10.1117/12.737318, 2007b.

Mertens, C. J., et al., SABER observations of mesospheric temperatures and comparisons with rocket falling sphere measurements taken during the 2002 summer MaCWAVE campaign, Geophys. Res. Lett., 31, L03105, doi: 10.1029/2003GL018605, 2004.

Mertens, C. J., M. G. Mlynczak, M. López-Puertas, P. P. Wintersteiner, R. H. Picard, J. R. Winick, L. L. Gordley, and J. M. Russell III, Retrieval of kinetic temperature and carbon dioxide abundance from non-local thermodynamic equilibrium limb emission measurements made by the SABER instrument on the TIMED satellite, in *Proceedings of SPIE, Remote Sensing of Clouds*

and the Atmosphere VII, Agia Pelagia, Crete, Greece, September 24-27, vol. 4882, 162-171, 2002.

Mertens, C. J., M. G. Mlynczak, M. López-Puertas, P. P. Wintersteiner, R. H. Picard, J. R. Winick, L. L. Gordley, and J. M. Russell III, Retrieval of mesospheric and lower thermospheric kinetic temperature from measurements of CO_2 15 μm Earth limb emission under non-LTE conditions, Geophys. Res. Lett., 28(7), 1391-1394, 2001.

Mlynczak, M., et al., The natural thermostat of nitric oxide emission at 5.3 μm in the thermosphere observed during the solar storms of April 2002, Geophys. Res. Lett., 30(21), 2100, doi:1029/2003GL017693, 2003.

Mlynczak, M., et al., Energy transport in the thermosphere during the solar storms of April 2002, J. Geophys. Res., 110, A12S25, doi:10.1029/2005JA011142, 2005.

Newton, G. P., J. C. G. Walker, and P. H. E. Meijer, Vibrationally excited nitrogen in stable auroral red arcs and its effects on ionospheric recombination, J. Geophys. Res., 79(25), 3807-3818, 1974.

O'Neil, R. R., J. R. Winick, R. H. Picard, and M. Kendra, Auroral NO^+ 4.3 μm emission observed from the Midcourse Space Experiment: Multiplatform observations of 9 February 1997, J. Geophys. Res., 112, A06327, doi:10.1029/2006JA012120, 2007.

Picard, R. H., J. R. Winick, R. D. Sharma, A. S. Zachor, P. J. Espy, and C. R. Harris, Interpretation of infrared measurements of the high-latitude thermosphere from a rocket-borne interferometer, Adv. Space Res., 7(10), 23-30, 1987.

Rees, M. H., *Physics and chemistry of the upper atmosphere*, Cambridge University Press, New York, 1989.

Richards, P. G., On the increase in nitric oxide density at midlat-

itudes during ionospheric storms, J. Geophys. Res., 109, A06304, doi:10.1029/2003JA010110, 2004.

Richards, P. G., Ion and neutral density variations during ionospheric storms in September 1974: Comparison of measurement and models, J. Geophys. Res., 107(A11), 1361, doi: 10.1029/2002JA00978, 2002.

Roble, R. G., Energetics of the mesosphere and thermosphere, in The Upper Mesosphere and Lower Thermosphere: A Review of Experiment and Theory, AGU Monograph Series, Vol. 87, edited by R. M. Johnson and T. L. Killeen, American Geophysical Union, Washington DC, 1995.

Rothman, L. S., et al., The HITRAN molecular spectroscopic database: edition of 2000 including updates through 2001, J. Quant. Spectrosc. Radiat. Transfer, 82, 5-44, 2003.

Russell, J. M., III, M. G. Mlynczak, L. L. Gordley, J. Tansock, and R. Esplin, An overview of the SABER experiment and preliminary calibration results, in *Proceedings of the SPIE, 44th Annual Meeting*, Denver, Colorado, July 18-23, vol. 3756, pp. 277-288, 1999.

Smith, M. A., V. M. Bierbaum, and S. R. Leone, Infrared chemiluminescence from vibrationally excited NO^+: Product branching in the $N^+ + O_2$ ion-molecule reactions, Chem. Phys. Lett., 94(4), 398-403, 1983.

Smith, D., R., E. R. Huppi, and J. O. Wise, Observation of highly rotationally excited NO^+ emission in the thermosphere, J. Atmos. Solar-Terr. Physics, 62, 1189-1198, 2000.

Strickland, D. J., D. L. Book, T. P. Coffey, and J. A. Fedder, Transport equation techniques for the deposition of auroral electrons, J. Geophys. Res., 81(16), 2755-2764, 1976.

Torr, M. R., D. G. Torr, P. G. Richards, and S. P. Yung, Mid- and low-latitude model of thermospheric emissions 1. $O^+(^2P)$ 7320 Å and $N_2(^2P)$ 3371 Å, J.

Geophys. Res., 95(A12), 21,147-21,168, 1990.

Werner, H.-J., and P. Rosmus, Ab initio calculations of radiative transition probabilities in the $X^1\Sigma^+$ ground state of the NO^+ ion, J. Molec. Spectrosc., 96, 362-367, 1982.

Winick, J. R., R. H. Picard, R. A. Joseph, R. D. Sharma, and P. P. Wintersteiner, An infrared spectral radiance code for the auroral thermosphere (AARC), *Rep. AFGL-TR-87-0334 (NTIS ADA202432)*, Air Force Geophysical Laboratory, Hanscom Air Force Base, Massachusetts, 1987.

Zaragoza, G., M. López-Puertas, M. A. Lopez-Valverde, and F. W. Taylor, Global distribution of CO_2 in the upper mesosphere as derived from UARS/ISAMS measurements, J. Geophys. Res., 105(D15), 19,829-19,839, 2000.

Zhang, Y., L. J. Paxton, D. Morrison, B. Wolven, H. Kil, and S. Wing, Nightside detached auroras due to precipitating protons/ions during intense magnetic storms, J. Geophys. Res., 110, A02206, doi: 10.1020/2004JA010498, 2005.

Table 1

$NO^+(v)$ Chemistry Model. Reference abbreviations are defined in section 3.1

Reaction Number	Reaction Process	Rate Coefficient (cm^3/s)	Reference (Rate Coeff)	Nascent $NO^+(v)$ Distribution
1	$N_2^+ + O$	$1.4 \times 10^{-10}(T_i/300)^{-0.44}$ $T_i \leq 1500$ K	MF74	WK87
		$5.2 \times 10^{-11}(T_i/300)^{0.20}$ $T_i > 1500$ K		
2	$N^+ + O_2$	2.7×10^{-10}	SM83	SM83
3	$O^+ + N_2$	$1.2 \times 10^{-12}(T_i/300)^{-1}$ $T_i \leq 750$ K	MF73	DS00
		$8.0 \times 10^{-14}(T_i/300)^{2}$ $T_i > 750$ K		
4	$O_2^+ + NO$	4.5×10^{-10}	LD74	MT08
5	$NO^+(v) + N_2$	7.0×10^{-12}	DO83	N/A

Fig. 1. SABER 4.3 μm limb radiance measurements during the April 2002 and Halloween 2003 solar storms. The blue lines are radiances profiles prior to the onset of the storms while the red lines are radiance profiles observed during the peaks of the storms. The dashed lines are the noise equivalent radiance (NER) level for the SABER 4.3 μm channel.

Fig. 2. NOAA/POES in-situ measurements of total energy flux (ergs/cm^2/s) and SABER-derived $NO^+(v)$ Volume Emission Rates (VER) (x 10^{-9} ergs/cm^3/s) in the northern hemisphere on October 30, 2003. The data are shown in magnetic coordinates (magnetic latitude and magnetic local time (MLT)). The NOAA/POES data are gridded as described in section 2 and shown in 3-hour UT-time intervals. The SABER-derived $NO^+(v)$ VER are shown at 110 km for orbits that fall within the corresponding 3-hour UT-time intervals of the POES data.

Fig. 3. FLIP model simulation of ion/neutral densities for April 2002, a representative quiet day and a day of peak solar-geomagnetic activity. The auroral dosing parameters used for the simulation shown in the second row are consistent with the maximum daily-averaged auroral electron dosing parameters observed by NOAA/POES on 20 April, 2002: total electron energy flux is 9 ergs/cm^2/s and the characteristic energy is 6 keV.

Fig. 4. Comparison of FLIP electron density (i.e., [e]) simulations with ground-based VHF incoherent scatter radar electron density measurements taken by the EISCAT facility at Tromsø, Norway from June 14-19, 2004. The first, second, and third panels correspond to the HP-index, AE-index, and kp-index, respectively. The bottom panel shows the actual FLIP/EISCAT [e] (cm^{-3}) comparisons at 115 km. The grey symbols in the bottom panel represent the individual EISCAT measurements ($\sim$ 1-minute average). The blue line represents the EISCAT 1-hour average [e]. The red line is the FLIP [e] simulation written out in 1-hour intervals.

Fig. 5. Simulations of 4.3 μm limb emission during quiescent and auroral conditions. The auroral conditions are the same as described in figure 3.

Fig. 6. SABER version 1.06 zonal mean CO_2(vmr) for July 2002, January and September 2003.

Fig. 7. Radiance simulation of SABER 4.3 μm channel, with and without NO^+(v) contribution.

Fig. 8. Temperature retrieval with anomalous polar summer CO_2 profile versus temperature retrieval using SABER-CO_2 mean profile at 41N.

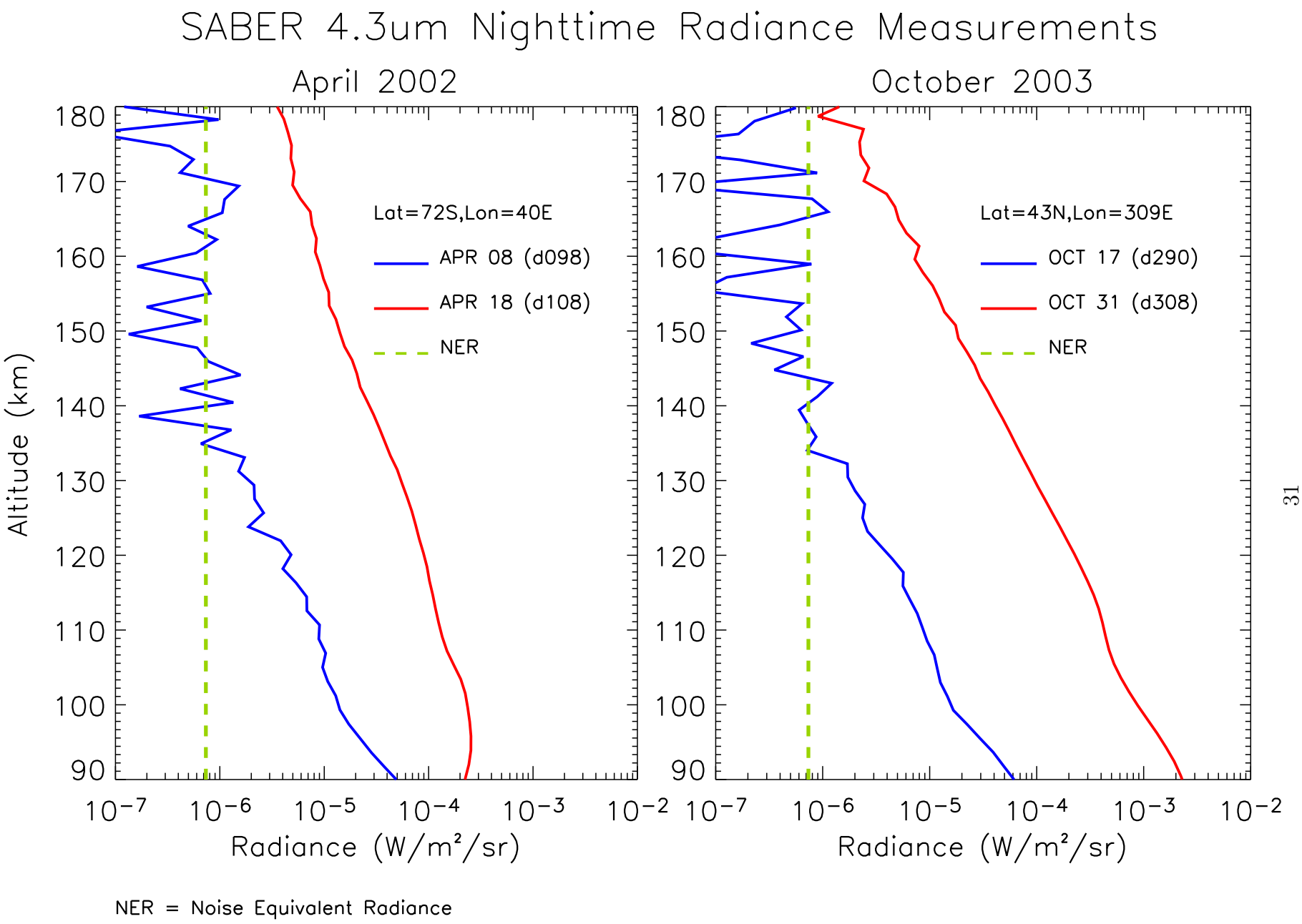
SABER 4.3um Nighttime Radiance Measurements
April 2002
October 2003
Altitude (km)
180
170
160
150
140
130
120
110
100
90
Lat=72S,Lon=40E
APR 08 (d098)
APR 18 (d108)
NER
Lat=43N,Lon=309E
OCT 17 (d290)
OCT 31 (d308)
NER
10⁻⁷
10⁻⁶
10⁻⁵
10⁻⁴
10⁻³
10⁻²
Radiance (W/m²/sr)
NER = Noise Equivalent Radiance

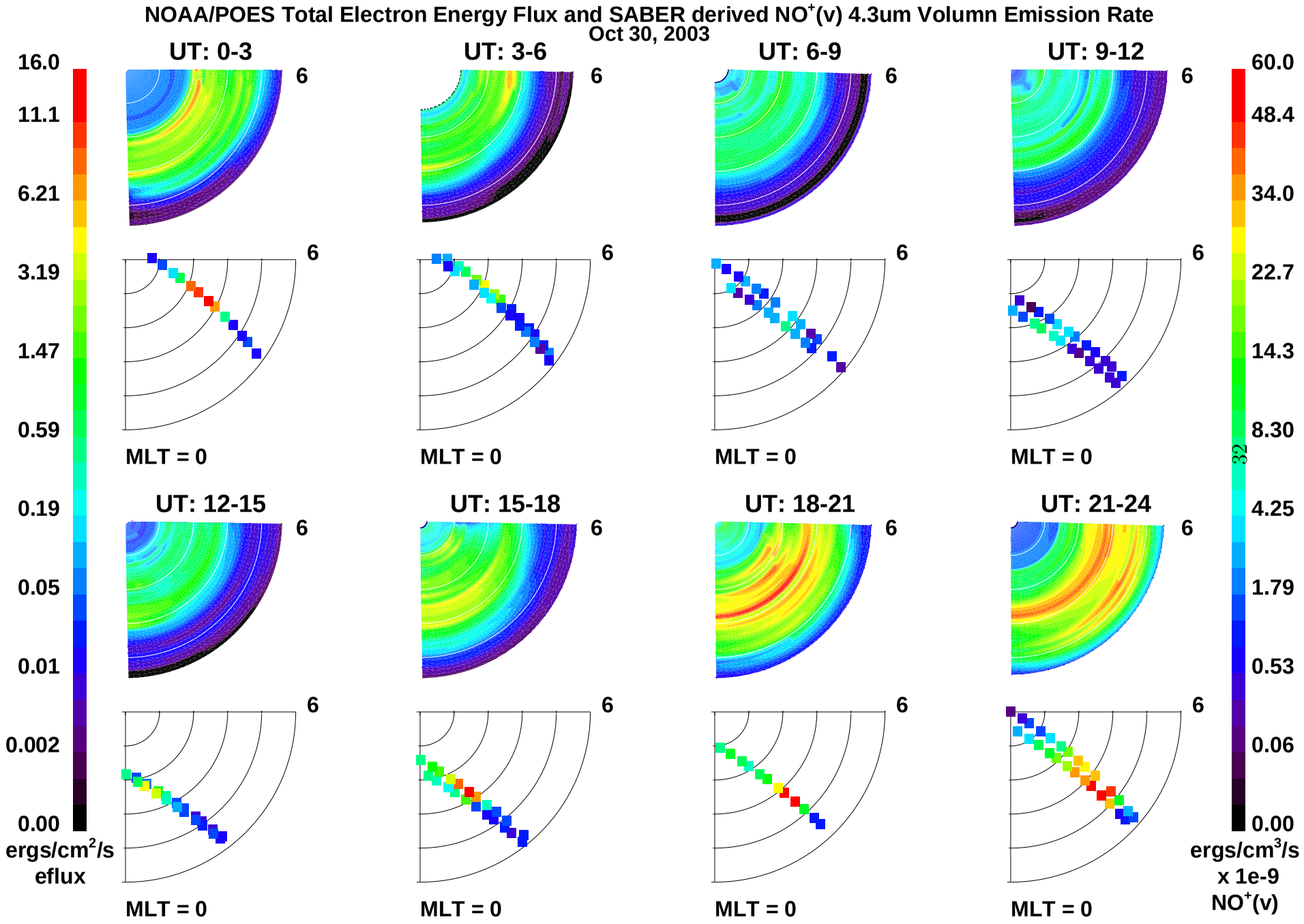
NOAA/POES Total Electron Energy Flux and SABER derived NO+(v) 4.3um Volumn Emission Rate
Oct 30, 2003
UT: 0-3
UT: 3-6
UT: 6-9
UT: 9-12
UT: 12-15
UT: 15-18
UT: 18-21
UT: 21-24
6
MLT = 0
16.0
11.1
6.21
3.19
1.47
0.59
0.19
0.05
0.01
0.002
0.00
ergs/cm2/s
eflux
60.0
48.4
34.0
22.7
14.3
8.30
4.25
1.79
0.53
0.06
0.00
ergs/cm3/s
x 1e-9
NO+(v)

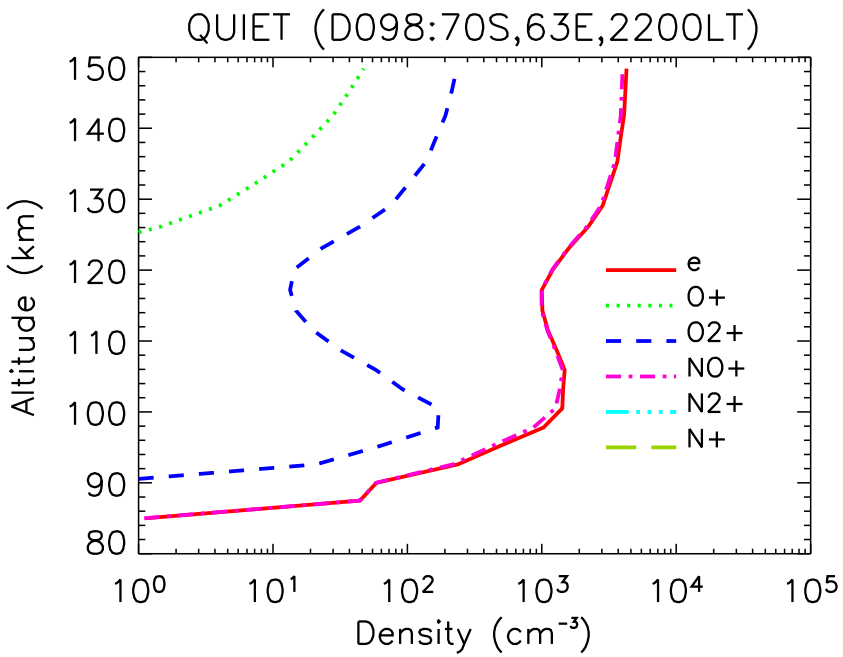
QUIET (D098:70S,63E,2200LT)
Altitude (km)
Density (cm⁻³)
e
O+
O2+
NO+
N2+
N+

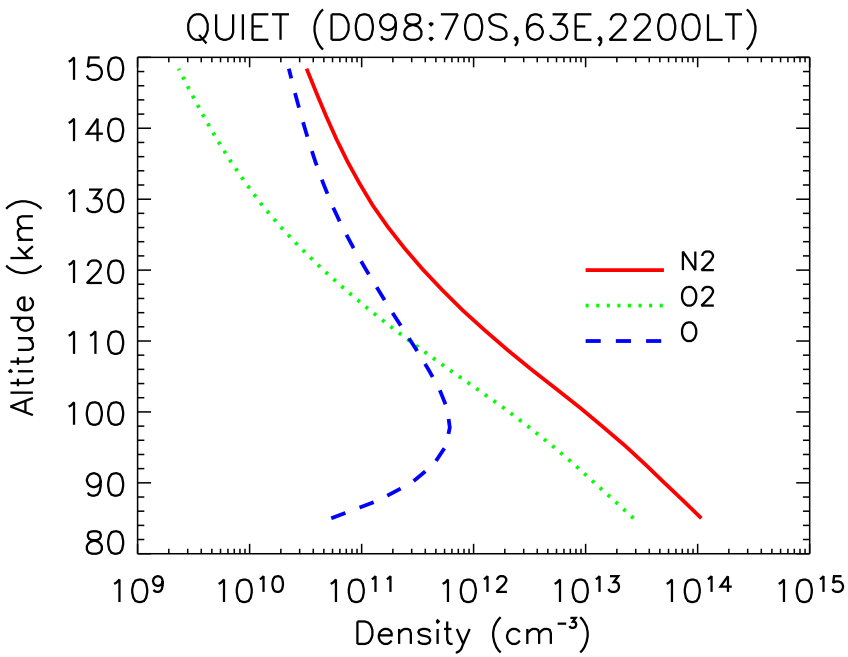
QUIET (D098:70S,63E,2200LT)
Altitude (km)
Density (cm⁻³)
N2
O2
O

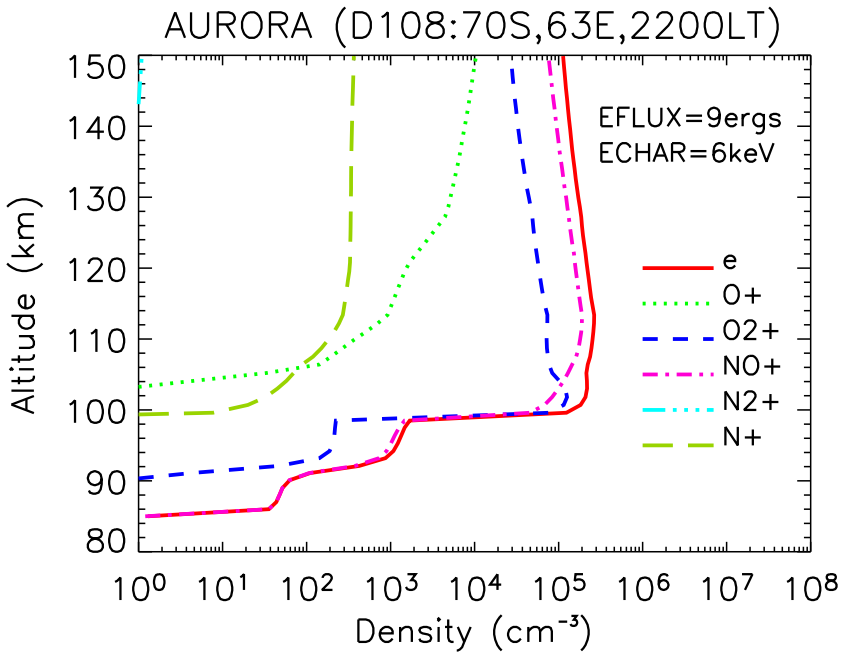
AURORA (D108:70S,63E,2200LT)
EFLUX=9ergs
ECHAR=6keV
Altitude (km)
Density (cm⁻³)
e
O+
O2+
NO+
N2+
N+

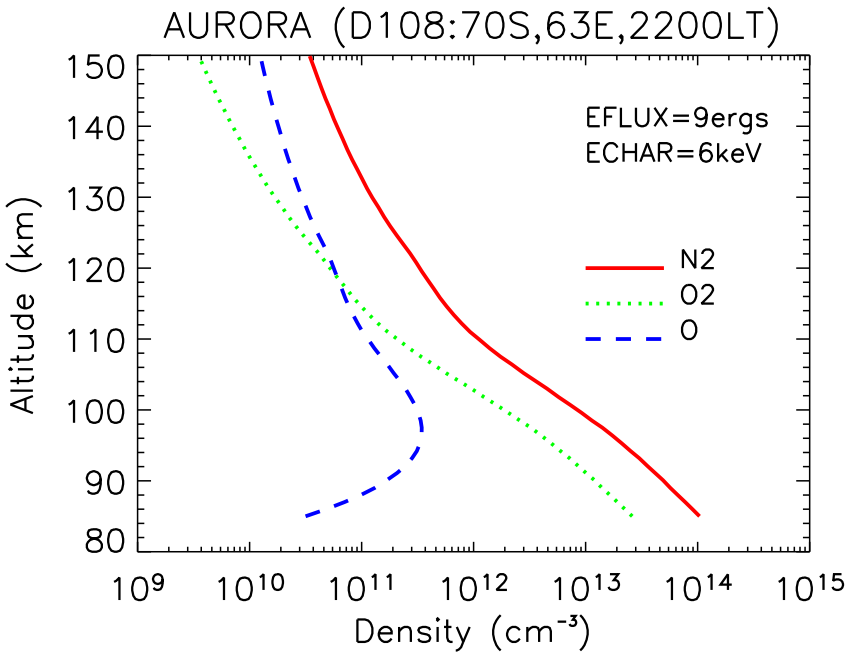
AURORA (D108:70S,63E,2200LT)
EFLUX=9ergs
ECHAR=6keV
Altitude (km)
Density (cm⁻³)
N2
O2
O

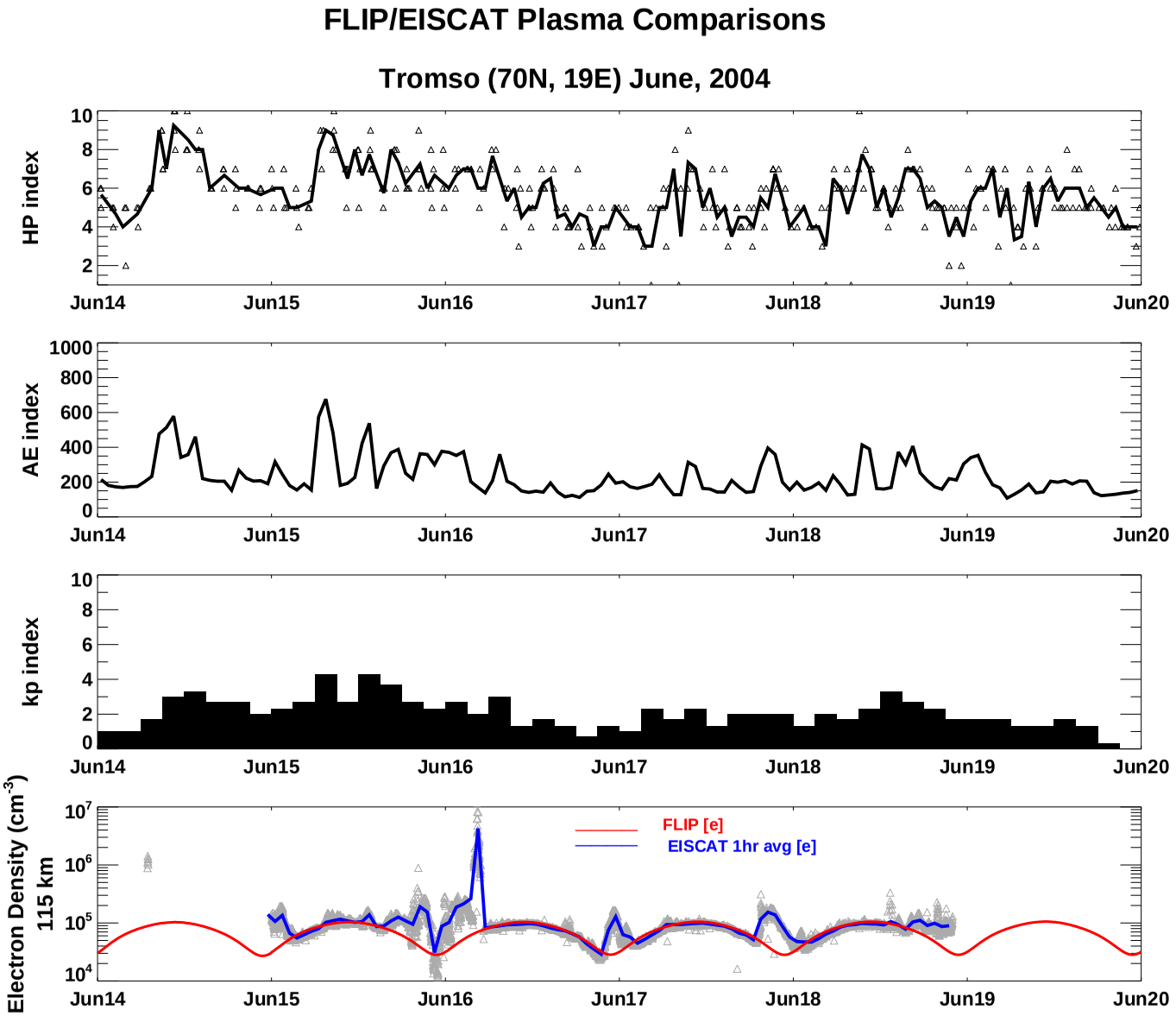
FLIP/EISCAT Plasma Comparisons
Tromso (70N, 19E) June, 2004
HP index
AE index
kp index
Electron Density (cm-3)
115 km
FLIP [e]
EISCAT 1hr avg [e]
Jun14
Jun15
Jun16
Jun17
Jun18
Jun19
Jun20

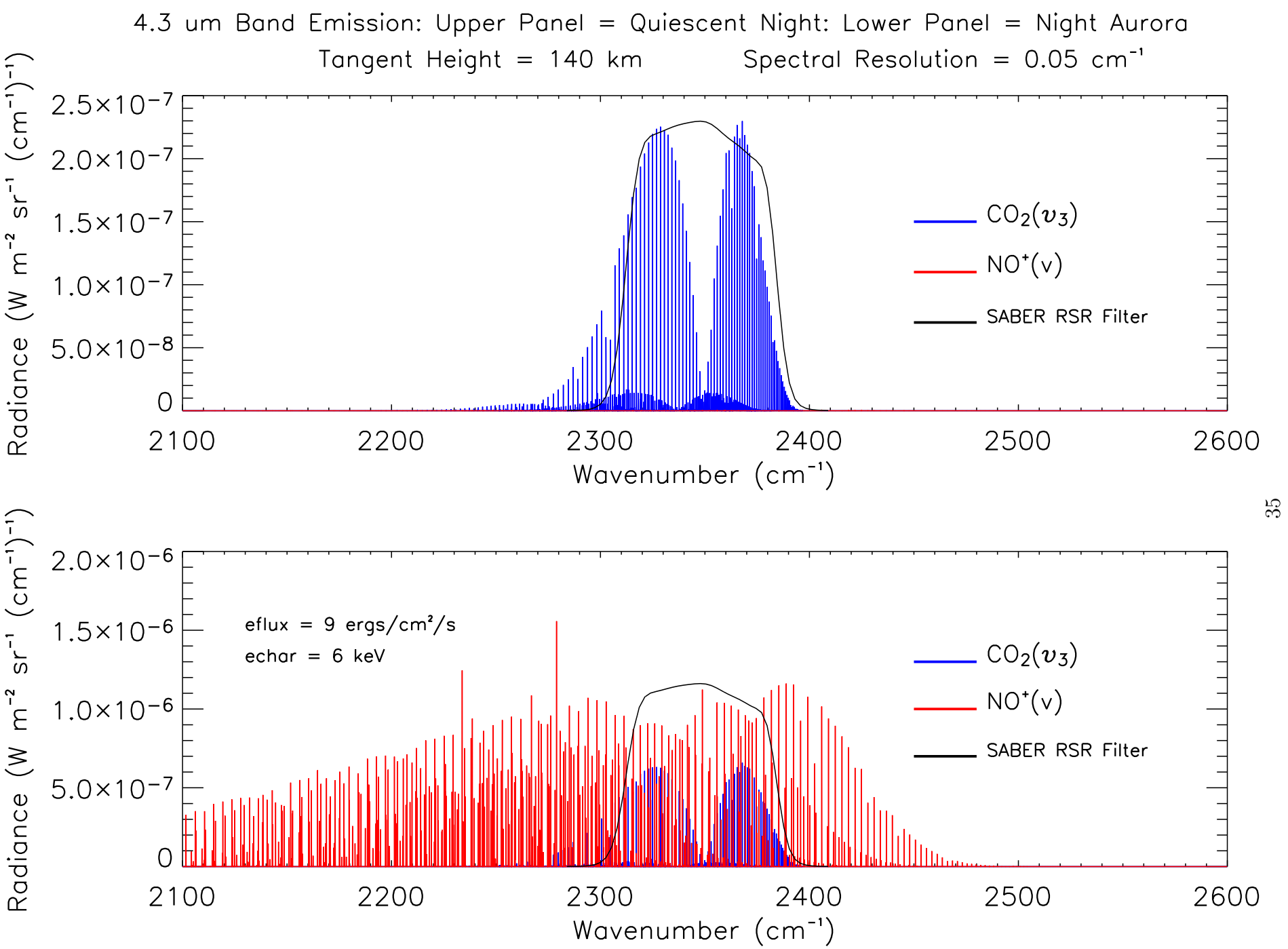
4.3 um Band Emission: Upper Panel = Quiescent Night: Lower Panel = Night Aurora
Tangent Height = 140 km
Spectral Resolution = 0.05 cm⁻¹
Radiance (W m⁻² sr⁻¹ (cm⁻¹)⁻¹)
2.5×10⁻⁷
2.0×10⁻⁷
1.5×10⁻⁷
1.0×10⁻⁷
5.0×10⁻⁸
0
2100
2200
2300
2400
2500
2600
Wavenumber (cm⁻¹)
CO2(υ3)
NO+(v)
SABER RSR Filter
Radiance (W m⁻² sr⁻¹ (cm⁻¹)⁻¹)
2.0×10⁻⁶
1.5×10⁻⁶
1.0×10⁻⁶
5.0×10⁻⁷
0
eflux = 9 ergs/cm²/s
echar = 6 keV
2100
2200
2300
2400
2500
2600
Wavenumber (cm⁻¹)
CO2(υ3)
NO+(v)
SABER RSR Filter

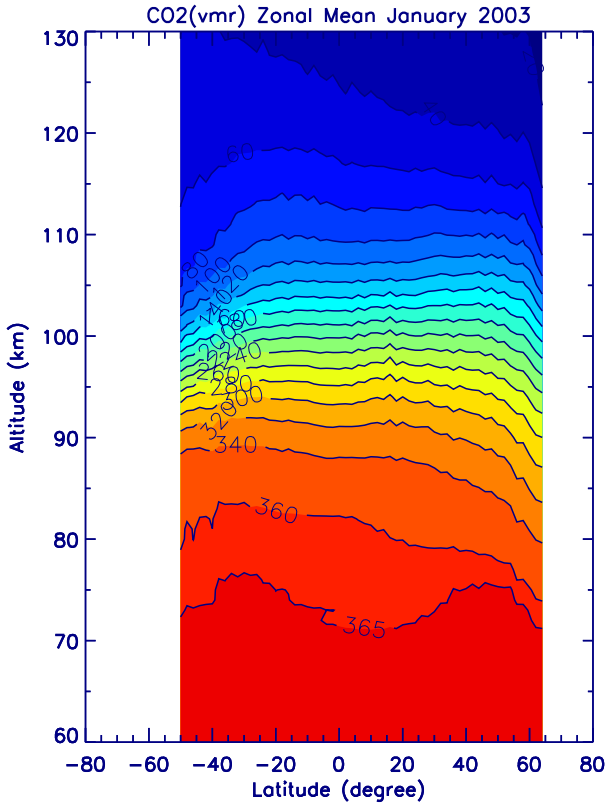
CO2(vmr) Zonal Mean January 2003
Altitude (km)
Latitude (degree)
130
120
110
100
90
80
70
60
−80 −60 −40 −20 0 20 40 60 80
60
80
100
120
140
160
180
200
220
240
260
280
300
320
340
360
365

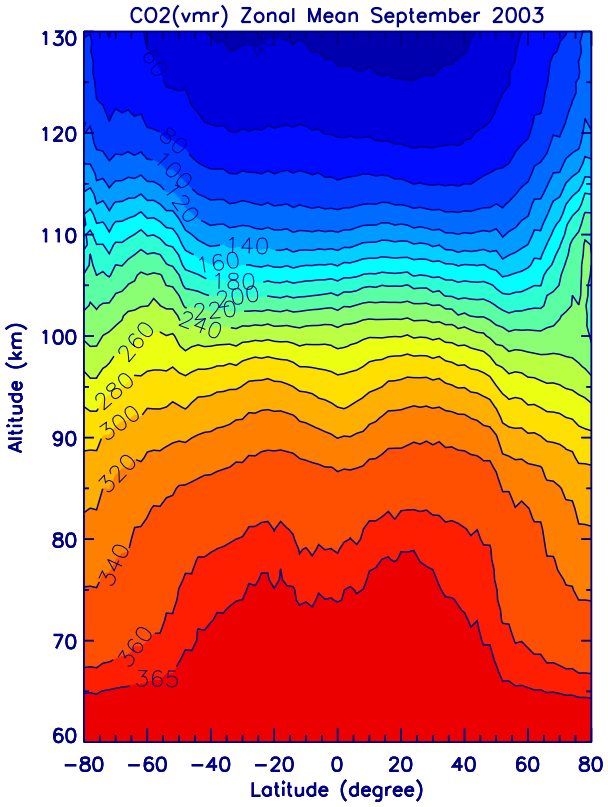
CO2(vmr) Zonal Mean September 2003
Altitude (km)
Latitude (degree)
130
120
110
100
90
80
70
60
−80 −60 −40 −20 0 20 40 60 80
60
80
100
120
140
160
180
200
220
240
260
280
300
320
340
360
365

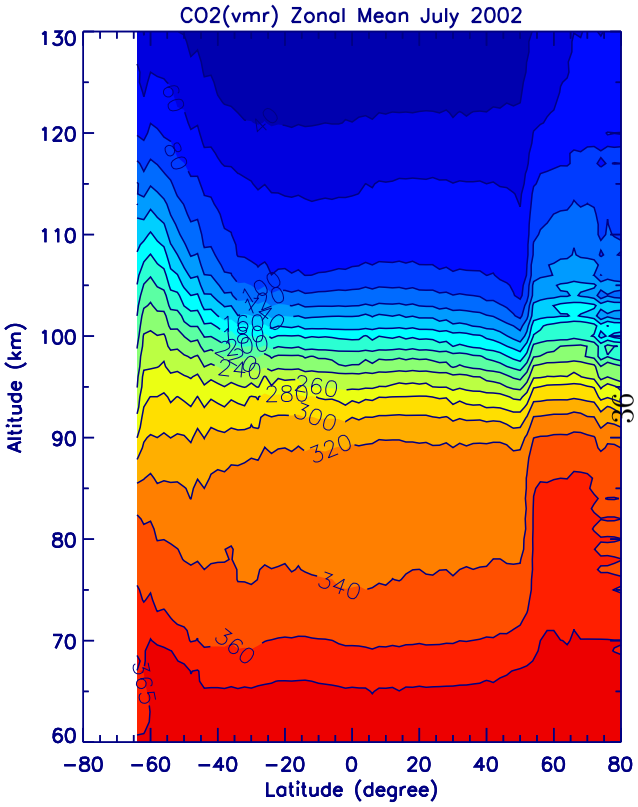
CO2(vmr) Zonal Mean July 2002
Altitude (km)
Latitude (degree)
130
120
110
100
90
80
70
60
−80 −60 −40 −20 0 20 40 60 80
60
80
100
120
140
160
180
200
220
240
260
280
300
320
340
360
365

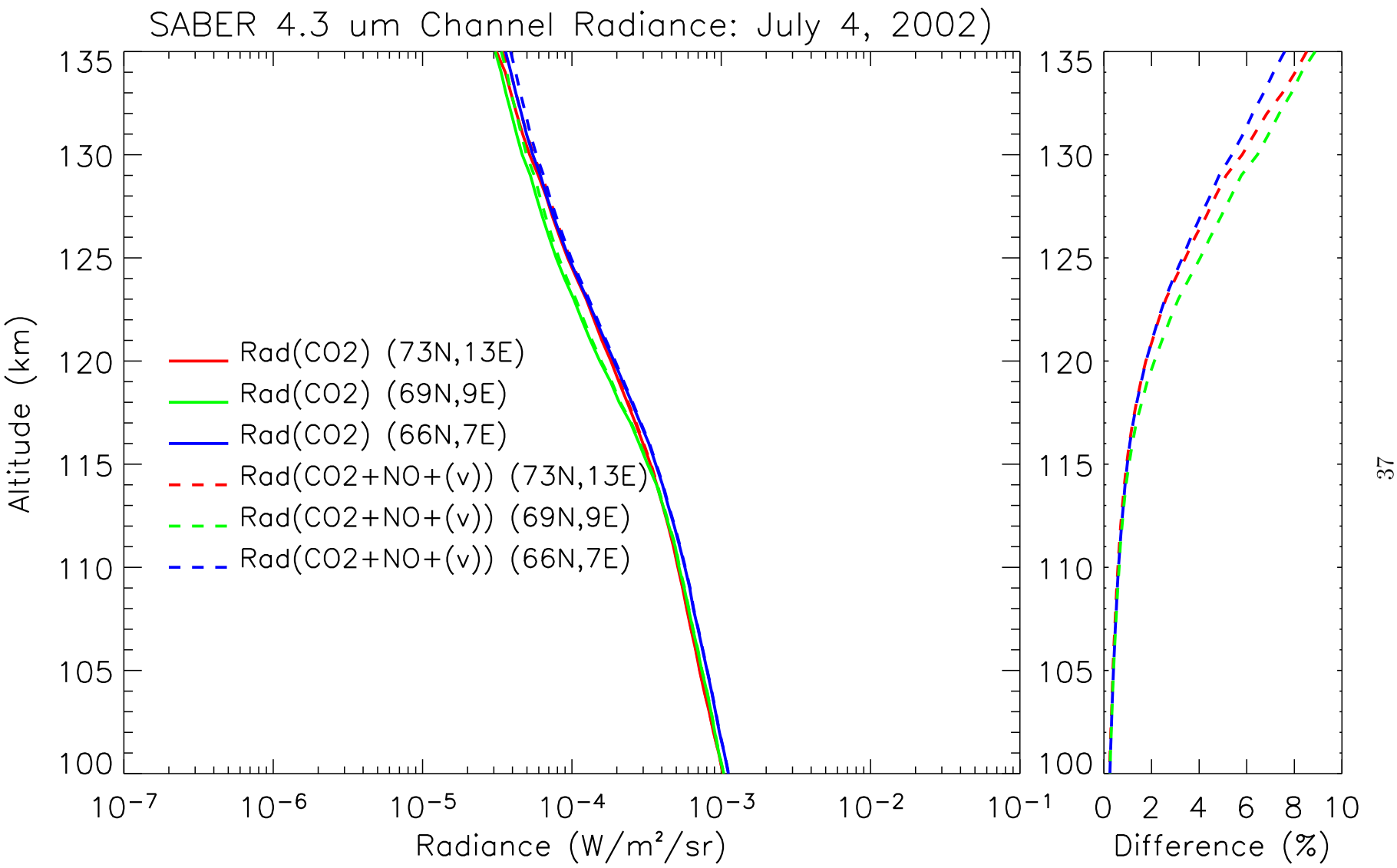
SABER 4.3 um Channel Radiance: July 4, 2002)
Altitude (km)
135
130
125
120
115
110
105
100
Rad(CO2) (73N,13E)
Rad(CO2) (69N,9E)
Rad(CO2) (66N,7E)
Rad(CO2+NO+(v)) (73N,13E)
Rad(CO2+NO+(v)) (69N,9E)
Rad(CO2+NO+(v)) (66N,7E)
10⁻⁷
10⁻⁶
10⁻⁵
10⁻⁴
10⁻³
10⁻²
10⁻¹
Radiance (W/m²/sr)
0 2 4 6 8 10
Difference (%)

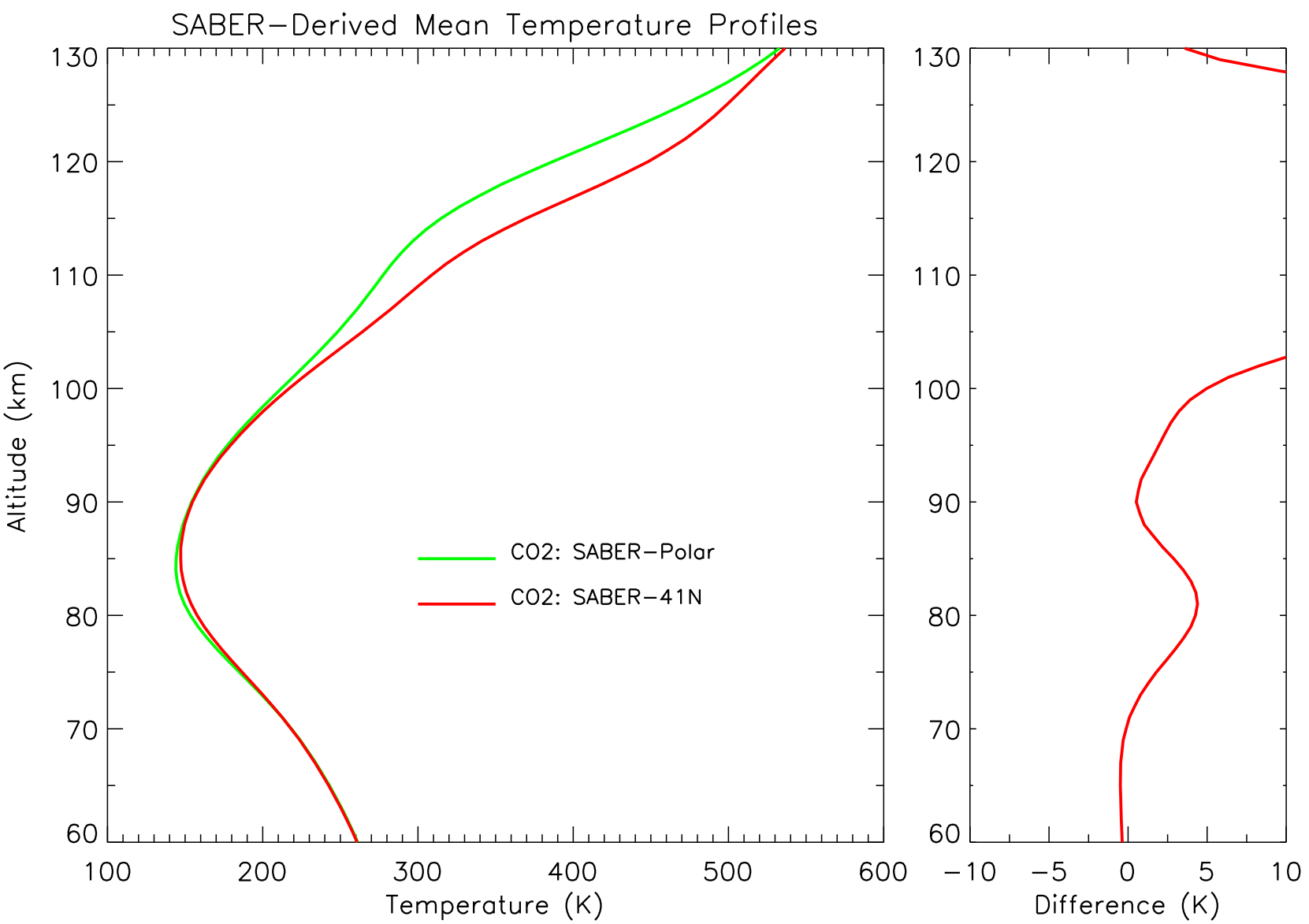
SABER–Derived Mean Temperature Profiles
Altitude (km)
130
120
110
100
90
80
70
60
100
200
300
400
500
600
Temperature (K)
CO2: SABER–Polar
CO2: SABER–41N
−10
−5
0
5
10
Difference (K)